A Multiplicative Regularized Gauss–Newton Inversion for Shape and Location Reconstruction

Puyan Mojabi, *Member, IEEE*, Joe LoVetri, *Senior Member, IEEE*, and Lotfollah Shafai, *Life Fellow, IEEE*

***Abstract*—A multiplicative regularized Gauss–Newton inversion algorithm is proposed for shape and location reconstruction of homogeneous targets with known permittivities. The data misfit cost functional is regularized with two different multiplicative regularizers. The first regularizer is the weighted L_2-norm total variation which provides an edge-preserving regularization. The second one imposes *a priori* information about the permittivities of the objects being imaged. Using both synthetically and experimentally collected data sets, we show that the proposed algorithm is robust in reconstructing the shape and location of homogeneous targets.**

***Index Terms*—Gauss–Newton inversion, microwave tomography, regularization.**

I. Introduction

In some applications of microwave tomography, there may exist *a priori* information about the objects being imaged. Proper incorporation of such information into the utilized inversion algorithm can improve reconstruction results as compared to the results obtained from *blind* inversion algorithms. There are different ways of incorporating such information into the inversion algorithm; e.g., by introducing a dummy variable over which to perform minimization [1], [2] or by utilizing an appropriate regularization term [3], [4].

In this paper, we consider one type of *a priori* information and attempt to incorporate it within the Gauss–Newton inversion algorithm via an appropriate regularization term. The *a priori* information considered herein is that the object of interest (OI) consists of some homogeneous scatterers with known permittivity values. The goal is then to find the shape and location of these scatterers. This problem is sometimes referred to as shape and location reconstruction. This approach can be very useful for nondestructive testing applications such as detection of voids in concrete [5], [6]. For the so-called binary shape and location reconstruction, where all the homogeneous scatterers have the same known permittivity value, Crocco and Isernia [4] introduced an additive regularizer for the contrast source inversion (CSI) algorithm which pushes each pixel in the discretized imaging domain to have either a contrast corresponding to the known permittivity value of the scatterers or a contrast of zero. Allowing the inversion algorithm to converge to a zero contrast is important as part of the imaging domain which is not occupied by the OI has the contrast of zero. Thus, the binary inversion algorithm attempts to find the spatial distribution of these two different contrasts within the imaging domain. The weight of this additive regularizer was chosen using an *ad hoc* algorithm [4]. Based on this algorithm, Abubakar and van den Berg [3] introduced a multiplicative regularizer (MR) which can provide an adaptive regularization [7] in the framework of the CSI algorithm. They also extended their algorithm for the case when there are several homogeneous targets inside the imaging domain. That is, it is more than a binary inversion algorithm which is only capable of reconstructing the shape and location of some homogeneous targets with the same known permittivity value.

Inspired by the work of Abubakar and van den Berg [3], we introduce a Gauss–Newton inversion (GNI) algorithm for shape and location reconstruction. As will be seen, the proposed algorithm is capable of incorporating *a priori* information about several homogeneous targets inside the imaging domain. The proposed inversion algorithm utilizes two different MRs. The first one is the weighted L_2-norm total variation which provides an edge-preserving regularization. The second regularizer, which is similar to the one used in the CSI algorithm for shape and location reconstruction, attempts to push the GNI algorithm to select one of the known permittivity values in any particular region of the imaging domain. Using both synthetically and experimentally collected data, we show that the proposed algorithm is robust in reconstructing the shape and location of homogeneous targets. Within the framework of this paper, we consider the 2-D transverse magnetic (TM) formulation and assume a time factor of $\exp(-j\omega t)$.

The paper is organized as follows. The mathematical formulation of the microwave tomography problem within the framework of the GNI algorithm is presented in Section II. The multiplicative regularized Gauss–Newton inversion algorithm, a blind inversion algorithm, is briefly explained in Section III. In Section IV, we present the proposed Gauss–Newton inversion algorithm for shape and location reconstruction. Sections V and VI provide the reconstruction results. Conclusions are provided in Section VII.

II. Problem Formulation

Consider a bounded imaging domain $\mathcal{D}$ which contains a nonmagnetic OI. Denoting the relative complex permittivity of the homogeneous background medium by ϵ_b, the complex contrast function is defined as

$$\chi(\boldsymbol{r}) \triangleq \frac{\epsilon_r(\boldsymbol{r}) - \epsilon_b}{\epsilon_b} \tag{1}$$

where $\boldsymbol{r} \in \mathcal{D}$ is the position vector.

Manuscript received October 05, 2010; revised May 09, 2011; accepted June 16, 2011. Date of publication August 18, 2011; date of current version December 02, 2011. This work was supported by the Natural Sciences and Engineering Research Council of Canada.

The authors are with the Department of Electrical and Computer Engineering, University of Manitoba, Winnipeg, MB R3T5V6 Canada (e-mail: Joe_LoVetri@umanitoba.ca).

Color versions of one or more of the figures in this paper are available online at http://ieeexplore.ieee.org.

Digital Object Identifier 10.1109/TAP.2011.2165487

The goal is to find the unknown contrast function $\chi(\boldsymbol{r})$ from the measured scattered field on the measurement domain $\mathcal{S}$ which is located outside the OI. To collect the scattered field data, the OI is successively interrogated by some known incident fields E_t^{inc} where t denotes the number of the active transmitter. Interaction of the incident field E_t^{inc} with the OI results in the total field E_t. Measuring incident and total electric fields on the measurement domain $\mathcal{S}$, the scattered electric field on $\mathcal{S}$ is found as $E_t^{\text{scat}} \triangleq E_t - E_t^{\text{inc}}$. The microwave tomography problem may then be formulated as the minimization over χ of the least squares data misfit cost functional

$$\mathcal{C}^{\text{LS}}(\chi) = \eta_{\mathcal{S}} \sum_{t=1}^{T_x} \left\| E_t^{\text{scat}}(\chi) - E_{\text{meas},t}^{\text{scat}} \right\|_{\mathcal{S}}^2 \tag{2}$$

where $E_t^{\text{scat}}(\chi)$ is the simulated scattered field on the measurement domain corresponding to the contrast χ and the tth transmitter, T_x is the total number of transmitters, and $\|\cdot\|_{\mathcal{S}}$ denotes the L_2-norm on $\mathcal{S}$. The weighting $\eta_{\mathcal{S}}$ is chosen to be

$$\eta_{\mathcal{S}} = \frac{1}{\sum_{t=1}^{T_x} \left\| E_{\text{meas},t}^{\text{scat}} \right\|_{\mathcal{S}}^2}. \tag{3}$$

The data misfit cost functional $\mathcal{C}^{\text{LS}}$ is nonlinear and ill-posed. The ill-posedness of the cost functional can be treated by different regularization techniques [7]. The nonlinearity of the problem is handled by utilizing iterative techniques such as the Gauss–Newton inversion (GNI) method. In the GNI algorithm, which is based on the Newton optimization but ignores the second derivative of the scattered electric field with respect to χ, the contrast at the nth iteration is updated as $\chi_{n+1} = \chi_n + \nu_n \Delta\chi_n$ where χ_n is the predicted contrast at the nth iteration, ν_n is an appropriate step-length, and $\Delta\chi_n$ is the correction.

In the discrete setup, we discretize the imaging domain $\mathcal{D}$ into N cells using 2-D pulse basis functions. Thus, the contrast function is represented by the complex vector $\underline{\chi} \in \mathbb{C}^N$. Assuming the number of measured data to be M, the measured scattered data on the discrete measurement domain $\mathcal{S}$ are denoted by the complex vector $\underline{E}_{\text{meas}}^{\text{scat}} \in \mathbb{C}^M$ which is the stacked version of the measured scattered fields for each transmitter. The vector $\underline{E}_n^{\text{scat}} \in \mathbb{C}^M$ is formed by stacking the discrete forms of $E_t^{\text{scat}}(\chi_n)$. The data misfit cost functional $\mathcal{C}^{\text{LS}}$ maps L_2 spaces of complex functions defined on $\mathcal{D}$ into a real number $(L_2(\mathcal{D}) \to \mathbb{R})$. The discrete form of this cost functional, which maps the complex vector $\underline{\chi}$ into a real number $(\mathbb{C}^N \to \mathbb{R})$, is denoted by the same symbol used in the continuous domain. That is, $\mathcal{C}^{\text{LS}}(\underline{\chi})$ represents the discrete form of $\mathcal{C}^{\text{LS}}(\chi)$.

III. Multiplicative Regularized Gauss–Newton Inversion (MR-GNI)

We may regularize the data misfit cost functional by the weighted L_2-norm total variation MR. This regularizer, which was first developed for the CSI algorithm [8], was recently adapted to the GNI algorithm [1], [7], [9], [10]. Utilizing this regularizer with the GNI method, we construct the following cost functional at the nth iteration of the algorithm:

$$\mathcal{C}_n(\chi) = \mathcal{C}^{\text{LS}}(\chi)\mathcal{C}_n^{\text{MR}}(\chi). \tag{4}$$

The weighted L_2-norm total variation MR $\mathcal{C}_n^{\text{MR}}$, which changes at each iteration of the algorithm, is given as [1], [7], [9]

$$\mathcal{C}_n^{\text{MR}}(\chi) = \frac{1}{A} \int_{\mathcal{D}} \frac{|\nabla\chi(\boldsymbol{r})|^2 + \delta_n^2}{|\nabla\chi_n(\boldsymbol{r})|^2 + \delta_n^2} d\boldsymbol{r} \tag{5}$$

where A is the area of the imaging domain and the gradient ∇ is taken with respect to the position vector $\boldsymbol{r}$. The steering parameter δ_n^2 is chosen to be [1], [9]

$$\delta_n^2 = \frac{\mathcal{C}^{\text{LS}}(\chi_n)}{\Delta A} \tag{6}$$

where ΔA is the area of a single cell in the uniformly discretized domain $\mathcal{D}$.

In the discrete domain, we minimize $\mathcal{C}_n(\underline{\chi})$ over the complex vector $\underline{\chi}$. The complex correction vector $\Delta\underline{\chi}_n$ may be found from [1], [7], [9]

$$\left(\underline{\boldsymbol{J}}_n^H \underline{\boldsymbol{J}}_n + \beta_n \underline{\boldsymbol{\mathcal{L}}}_n\right) \Delta\underline{\chi}_n = -\underline{\boldsymbol{J}}_n^H \underline{d}_n - \beta_n \underline{\boldsymbol{\mathcal{L}}}_n \underline{\chi}_n \tag{7}$$

where $\underline{\boldsymbol{J}}_n \in \mathbb{C}^{M\times N}$ is the Jacobian matrix. This matrix is formed by stacking $\underline{\boldsymbol{J}}_{t,n}$ matrices $(t = 1, \ldots, T_x)$ where $\underline{\boldsymbol{J}}_{t,n}$ represents the discrete form of the derivative of the scattered field with respect to the contrast and evaluated at $\chi = \chi_n$. That is, the matrix $\underline{\boldsymbol{J}}_{t,n}$ represents the discrete form of $(\partial E_t^{\text{scat}})/(\partial\chi)|_{\chi=\chi_n}$. The discrepancy vector $\underline{d}_n$ is given as

$$\underline{d}_n = \underline{E}_n^{\text{scat}} - \underline{E}_{\text{meas}}^{\text{scat}} \tag{8}$$

and $\beta_n = \|\underline{d}_n\|^2$. The regularization operator $\underline{\boldsymbol{\mathcal{L}}}_n$ represents the discrete form of the operator "$-\nabla \cdot b_n^2 \nabla$" where "$\nabla\cdot$" is the divergence operator and

$$b_n^2(\boldsymbol{r}) = A^{-1}(|\nabla\chi_n(\boldsymbol{r})|^2 + \delta_n^2)^{-1}. \tag{9}$$

We note that the weighted Laplacian operator "$-\nabla \cdot b_n^2 \nabla$" provides edge-preserving characteristics for the inversion algorithm [9], [11]. Also, it should be noted that the null space of the operator $\underline{\boldsymbol{\mathcal{L}}}_n$ does not intersect with that of $\underline{\boldsymbol{J}}_n^H \underline{\boldsymbol{J}}_n$ [see (7)], thus ensuring a unique solution at each iteration of the algorithm. (For more explanation, see [12, pp. 53–54].)

Having found the correction $\Delta\underline{\chi}_n$, the contrast is updated in the form of $\underline{\chi}_{n+1} = \underline{\chi}_n + \nu_n \Delta\underline{\chi}_n$ where ν_n is the step length determined via an appropriate line search algorithm. This completes the brief explanation of the multiplicative regularized Gauss–Newton inversion which we refer to as the MR-GNI method in this paper.

IV. Gauss–Newton Inversion for Shape and Location Reconstruction (SL-GNI)

Assume that the imaging domain $\mathcal{D}$ consists of L homogeneous targets, each of which has a known contrast of $\chi_\ell^{\text{h}} \in \mathbb{C}$ where $\ell = 1, \ldots, L$. The goal is to reconstruct the shape and location of these objects using the measured scattered field on $\mathcal{S}$. In the framework of the CSI algorithm, Abubakar and van den Berg proposed a multiplicative regularization term which pushes each pixel of the imaging domain to be one of these L known contrast values [3]. This MR can be written as

$$\mathcal{C}_n^{\text{hom}}(\chi) = \frac{1}{A} \int_{\mathcal{D}} \prod_{\ell=1}^{L} \frac{\left|\chi(\boldsymbol{r}) - \chi_\ell^{\text{h}}\right|^2 + \alpha_n^2}{\left|\chi_n(\boldsymbol{r}) - \chi_\ell^{\text{h}}\right|^2 + \alpha_n^2} d\boldsymbol{r}. \tag{10}$$

In their work, the steering parameter α_n^2 was chosen so that the regularization factor is more dominant as the number of CSI iterations increases [3].

In our work, we use the regularization term $\mathcal{C}_n^{\mathrm{hom}}$ in the framework of the GNI algorithm. To make the inversion algorithm more stable, we add one more level of regularization using the weighted L_2-norm total variation multiplicative regularization term $\mathcal{C}_n^{\mathrm{MR}}$. That is, we construct the regularized cost functional $\mathcal{C}_n^{\mathrm{shape}}(\chi)$ at the nth iteration of the inversion algorithm as

$$\mathcal{C}_n^{\mathrm{shape}}(\chi) = \mathcal{C}^{\mathrm{LS}}(\chi)\mathcal{C}_n^{\mathrm{hom}}(\chi)\mathcal{C}_n^{\mathrm{MR}}(\chi). \tag{11}$$

Thus, the data misfit cost functional $\mathcal{C}^{\mathrm{LS}}$ is regularized with two different multiplicative regularization terms: $\mathcal{C}_n^{\mathrm{MR}}$ and $\mathcal{C}_n^{\mathrm{hom}}$. The latter imposes the *a priori* information about the OI. The former is mainly used to impose the weighted Laplacian operator $\underline{\underline{\boldsymbol{\mathcal{L}}}}_n$ at different iterations of the GNI algorithm so as to make the inversion algorithm more stable. To the best of our knowledge, it is the first time that two different MRs have been used to regularize the microwave tomography problem.

In our work, we choose the steering parameter α_n^2 to be

$$\alpha_n^2 = \mathcal{C}^{\mathrm{LS}}(\chi_n). \tag{12}$$

This choice for α_n^2 is similar to the choice of δ_n^2, both of which decrease as the predicted contrast converges to the true solution. The only difference between δ_n^2 and α_n^2 is that the former is dependent on ΔA whereas the latter is not. This can be justified by noting that δ_n^2 is added to $|\nabla\chi|^2$ [see (5)], which depends on the area of each pixel within the imaging domain. Thus, this choice of δ_n^2 minimizes the discretization dependency in the performance of $\mathcal{C}_n^{\mathrm{MR}}$. However, it is not the case for α_n^2 which is added to $|\chi(\boldsymbol{r}) - \chi_\ell^{\mathrm{h}}|^2$; see (10).

Minimizing $\mathcal{C}_n^{\mathrm{shape}}(\underline{\chi})$ over the complex vector $\underline{\chi}$, the complex correction vector $\Delta\underline{\chi}_n$ may be found from (see Appendix I for the derivation)

$$\left(\underline{\underline{\boldsymbol{J}}}_n^H\underline{\underline{\boldsymbol{J}}}_n + \beta_n\underline{\underline{\boldsymbol{\mathcal{L}}}}_n + \beta_n\sum_{\ell=1}^{L}\underline{\underline{\boldsymbol{D}}}_{\ell,n}\right)\Delta\underline{\chi}_n = -\underline{\underline{\boldsymbol{J}}}_n^H\underline{d}_n - \beta_n\underline{\underline{\boldsymbol{\mathcal{L}}}}_n\underline{\chi}_n - \beta_n\sum_{\ell=1}^{L}\underline{\underline{\boldsymbol{D}}}_{\ell,n}\left(\underline{\chi}_n - \chi_\ell^{\mathrm{h}}\underline{e}\right) \tag{13}$$

where $\underline{e} \in \mathbb{R}^N$ is a vector of all ones. The matrix $\underline{\underline{\boldsymbol{D}}}_{\ell,n} \in \mathbb{R}^{N\times N}$ is a diagonal matrix given as

$$\underline{\underline{\boldsymbol{D}}}_{\ell,n} = \mathrm{diag}\left(\frac{1}{A}\underline{\xi}_{\ell,n}^2\right) \tag{14}$$

where $\underline{\xi}_{\ell,n}^2 \in \mathbb{R}^N$ is the discretized form of

$$\xi_{\ell,n}^2(\boldsymbol{r}) = \left(\left|\chi_n(\boldsymbol{r}) - \chi_\ell^{\mathrm{h}}\right|^2 + \alpha_n^2\right)^{-1}. \tag{15}$$

As in the standard MR-GNI method, the contrast is updated as $\underline{\chi}_{n+1} = \underline{\chi}_n + \nu_n\Delta\underline{\chi}_n$ where ν_n is an appropriate step length. For both the MR-GNI method and the GNI method for shape and location reconstruction, we use the line search algorithm explained in [13] to find an appropriate step length. It should be noted that the computational complexity of the proposed GNI algorithm for shape and location reconstruction is similar to that of the MR-GNI method as $\underline{\underline{\boldsymbol{D}}}_{\ell,n}$ matrices are all diagonal. (The computational complexity analysis of the MR-GNI method can be found in [7, App. B].) This completes the brief explanation of the Gauss–Newton inversion for shape and location reconstruction. In this paper, we refer to this algorithm as the SL-GNI algorithm.

It is worth noting that this algorithm uses two different regularizers to improve the reconstruction results. In comparison, the CSI algorithm for shape and location reconstruction, herein referred to as the SL-CSI method, utilizes only the $\mathcal{C}_n^{\mathrm{hom}}$ regularizer [3]. From our experience with the GNI method, utilizing both $\mathcal{C}_n^{\mathrm{hom}}$ and $\mathcal{C}_n^{\mathrm{MR}}$ results in a more robust reconstruction than utilizing only the $\mathcal{C}_n^{\mathrm{hom}}$ regularizer. This will be shown in Sections V-B and VI-B. Moreover, although the shape and location regularizer $\mathcal{C}_n^{\mathrm{hom}}$ used in the SL-GNI method is similar to the one used in the SL-CSI algorithm, its incorporation into the GNI algorithm requires that the steering parameter α_n^2 be chosen in a different way. This is due to the fact that the steering parameter used in the SL-CSI algorithm is chosen to be the normalized error in the so-called domain equation [3, eq. 16]. However, in the SL-GNI algorithm, there is no explicit domain equation in the cost functional to be minimized. Thus, we choose the steering parameter α_n^2 to be $\mathcal{C}^{\mathrm{LS}}(\chi_n)$ so that this parameter decreases as the algorithm gets closer to the solution. We would also like to add that the main disadvantage of the SL-CSI method is that there is no closed-form formula to find the step length [3, p. 6] as opposed to the multiplicative regularized contrast source inversion (MR-CSI) method where the step length is found using a closed-form formula (see [8, eq. (33) and (41)]), thus, in the SL-CSI algorithm, a numerical line search algorithm needs to be used. This can increase the computational complexity of the SL-CSI significantly as this algorithm usually requires a few hundred iterations (the number of iterations is usually set to 1024 in the contrast source inversion algorithm). On the other hand, although both the SL-GNI and MR-GNI algorithms require numerical line searches to calculate the step length, the number of iterations for these two algorithms is much lower than that required for the SL-CSI and MR-CSI methods (the number of iterations is usually lower than 20 in both SL-GNI and MR-GNI methods). Thus, utilizing a numerical line search algorithm does not add a large computational burden to the SL-GNI and MR-GNI algorithms. Specially, if adaptive regularization, like the one used in our paper, is incorporated with an appropriate line search algorithm, the number of calls to the numerical line search algorithm is minimal in the GNI algorithm (for more discussion, see [14, Sec. V.D]).

V. Synthetic Data Results

In this section, we test the performance of the proposed algorithm against two different synthetically collected data sets. To avoid any inverse crime, the synthetic data sets are generated on a different grid than the ones used in the inversion algorithm.

We also add 3% root mean square (RMS) additive white noise to the synthetic data set using [15]

$$\underline{E}^{\text{scat}}_{\text{meas},t} = \underline{E}^{\text{scat,fwd}}_{t} + \max\left[\forall_t \underline{E}^{\text{scat,fwd}}_{t}\right] \frac{\eta}{\sqrt{2}}(\underline{\vartheta}_1 + j\underline{\vartheta}_2) \tag{16}$$

where $\underline{E}^{\text{scat,fwd}}_{t}$ is the scattered field on the measurement domain due to the tth transmitter obtained by the forward solver, $\underline{\vartheta}_1$ and $\underline{\vartheta}_2$ are two real vectors whose elements are uniformly distributed zero-mean random numbers between -1 and 1, and $\eta = 0.03$. The vector $\underline{E}^{\text{scat}}_{\text{meas}}$, constructed by stacking the vectors $\underline{E}^{\text{scat}}_{\text{meas},t}$, is then used to test the inversion algorithm against synthetic data sets. Finally, it should be mentioned that the starting guess for the contrast to be found is set to be zero in both MR-GNI and SL-GNI algorithms for these synthetic data sets.

In all examples, including the experimental data results, we ensure that we have at least ten cells per wavelength. We note that the proposed algorithm is robust with respect to oversampling of the unknown contrast. This is discussed in Appendix II.

A. Concentric Squares

We consider a similar scatterer which has been used in [14] and [16]–[18]. The scatterer consists of two concentric squares located in free space, the inner square having dimension of 0.3 m $\times$ 0.3 m with a relative complex permittivity of $1.6 + j0.2$, which corresponds to a contrast of $0.6 + j0.2$. The inner square is surrounded by an exterior square having dimension of 0.6 m $\times$ 0.6 m with a relative complex permittivity of $1.3 + j0.4$, which corresponds to a contrast of $0.3 + j0.4$. The exact relative complex permittivity profile is shown in Fig. 1. We consider this target in two different scenarios distinguished by their frequency of operation. In both scenarios, the synthetic data, which include 16 transmitters (line sources) and 16 receivers per transmitter evenly placed on the measurement circle $\mathcal{S}$ of radius 0.7 m, are generated using a grid of 80 $\times$ 80 square pulses in a 0.9 m $\times$ 0.9 m square. The imaging domain $\mathcal{D}$ is chosen to be a 0.94 m $\times$ 0.94 m and is discretized into 61 $\times$ 61 square pulses. It should also be noted that the contrast of the object being imaged is assumed to be the same in both frequencies of operation.

In the first scenario, the frequency of operation is chosen to be 100 MHz. The inversion of this data set using the MR-GNI method is shown in Fig. 2(a) and (b). As can be seen, the MR-GNI method is not capable of resolving the concentric squares. We also utilize the SL-GNI algorithm with three different values for χ^{h} which correspond to the true contrast values within the imaging domain; i.e., $\chi^{\text{h}}_1 = 0$, $\chi^{\text{h}}_2 = 0.6 + j0.2$, and $\chi^{\text{h}}_3 = 0.3 + j0.4$. Utilizing these three values for χ^{h}, the shape and location reconstruction of this target are shown in Fig. 2(c) and (d). Although the SL-GNI algorithm is not capable of reconstructing the square shape of the two scatterers, it does resolve two regions and provides a good location reconstruction. It is worth noting that the number of MR-GNI and SL-GNI iterations required for the convergence is 8 and 11, respectively. (The inversion algorithms are terminated when the difference between two successive data misfit values becomes less than 10^{-7}.) The inversion algorithms were implemented in object-oriented MATLAB® and were

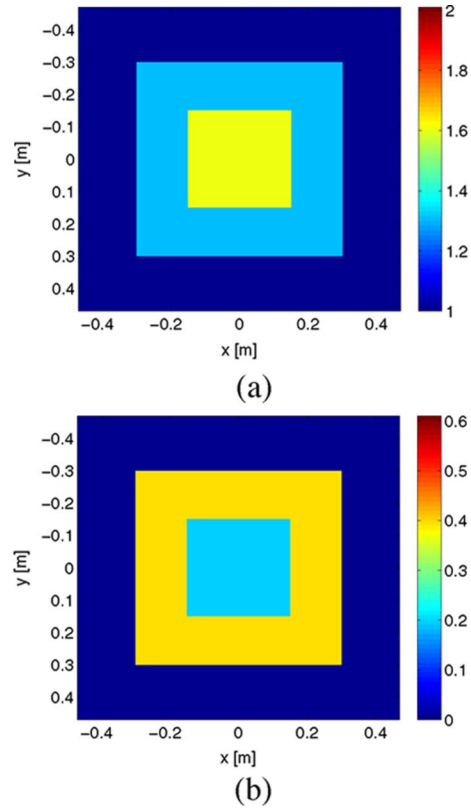

Fig. 1. Exact relative complex permittivity profile for the first synthetic test case (concentric squares): (a) $\text{Re}(\epsilon_r)$ and (b) $\text{Im}(\epsilon_r)$.

running on a PC workstation with two Intel® Xeon® quad-core 2.8-GHz processors. With this machine, the first iterations of the MR-GNI and SL-GNI algorithms took about 7 and 3 s, respectively. In the second scenario, we choose the frequency of operation to be 1 GHz. The MR-GNI reconstruction of this target as well as its SL-GNI reconstruction using the three true values for χ^{h} are shown in Fig. 3. As can be seen, both of these algorithms can reconstruct the scatterer very well at this frequency of operation.

To test the robustness of the SL-GNI algorithm to the chosen values for χ^{h}, we run this algorithm with 20% error in the utilized values for χ^{h}. Specifically, we assume $+20\%$ error in χ^{h}_2 and -20% error in χ^{h}_3. That is, we consider χ^{h}_2 and χ^{h}_3 to be $0.72 + j0.24$ and $0.24 + j0.32$, respectively. Of course, the value of χ^{h}_1, which corresponds to the contrast of the background medium, is kept to be 0. Utilizing these values for χ^{h}, the inversion results for the two frequencies of operation are shown in Fig. 4. As can be seen, the inversion results (shape and location) are very similar to the case where the true values of χ^{h} are incorporated to the SL-GNI algorithm.

In order to test the performance of the SL-GNI algorithm when the *a priori* information about the number of contrast values L is wrong, we consider two different cases. In the first case, an extra contrast value is given to the SL-GNI algorithm: in addition to $\chi^{\text{h}}_1 = 0$, $\chi^{\text{h}}_2 = 0.6 + j0.2$, and $\chi^{\text{h}}_3 = 0.3 + j0.4$, one extra contrast value χ^{h}_4 is also given to the algorithm. That is, we utilize a quaternary inversion algorithm instead of a trinary inversion algorithm. In Fig. 5(a)–(d), we have shown the performance of the SL-GNI algorithm for this situation for two different values of χ^{h}_4 at $f = 100$ MHz. For $\chi^{\text{h}}_4 = 0.45 + j0.3$,

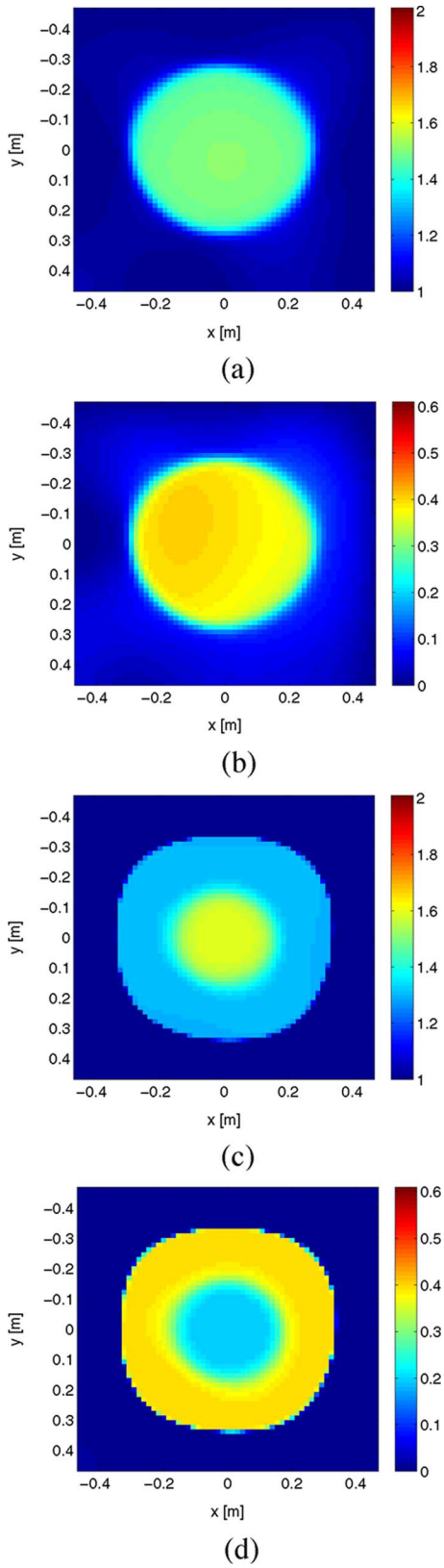

Fig. 2. Reconstruction of $\mathrm{Re}(\epsilon_r)$ and $\mathrm{Im}(\epsilon_r)$ of the concentric squares when the frequency of operation is $f = 100$ MHz: (a)–(b) the MR-GNI reconstruction, and (c)–(d) the SL-GNI reconstruction.

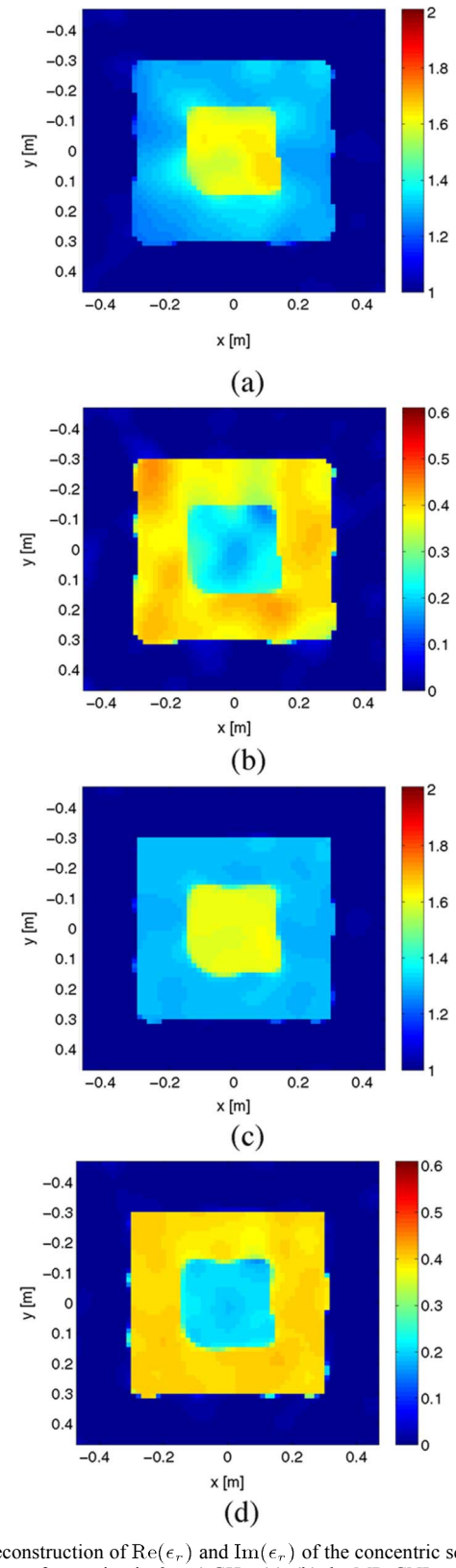

Fig. 3. Reconstruction of $\mathrm{Re}(\epsilon_r)$ and $\mathrm{Im}(\epsilon_r)$ of the concentric squares when the frequency of operation is $f = 1$ GHz: (a)–(b) the MR-GNI reconstruction, and (c)–(d) the SL-GNI reconstruction.

the algorithm resolves the two scatterers but converges to χ_4^{h} instead of χ_2^{h}. Also, the overall dimension of the reconstructed inner scatterer is wrong. For $\chi_4^{\mathrm{h}} = 0.9 + j0.6$, the inversion result is very similar to the one obtained using only the three true contrast values [see Fig. 2(c)–(d)].

In the second case, we give only two contrast values to the SL-GNI algorithm, as opposed to the three contrast values cor-

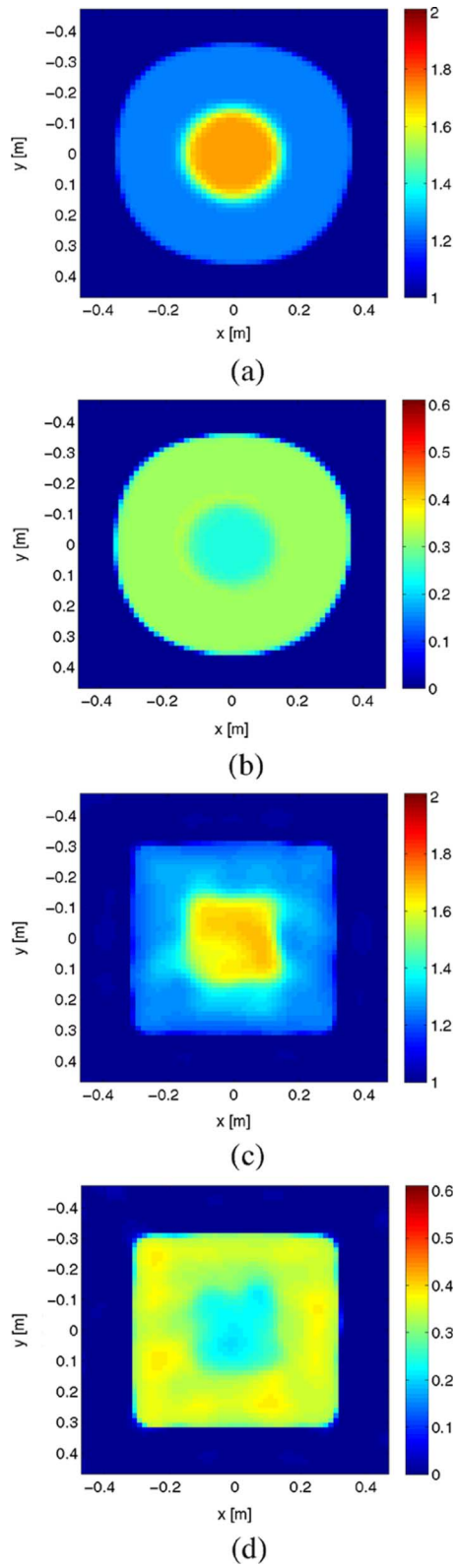

Fig. 4. The SL-GNI reconstruction of $\mathrm{Re}(\epsilon_r)$ and $\mathrm{Im}(\epsilon_r)$ of the concentric squares with 20% error in the utilized values for χ_ℓ^{h}: (a)–(b) when the frequency of operation is 100 MHz, and (c)–(d) when the frequency of operation is 1 GHz.

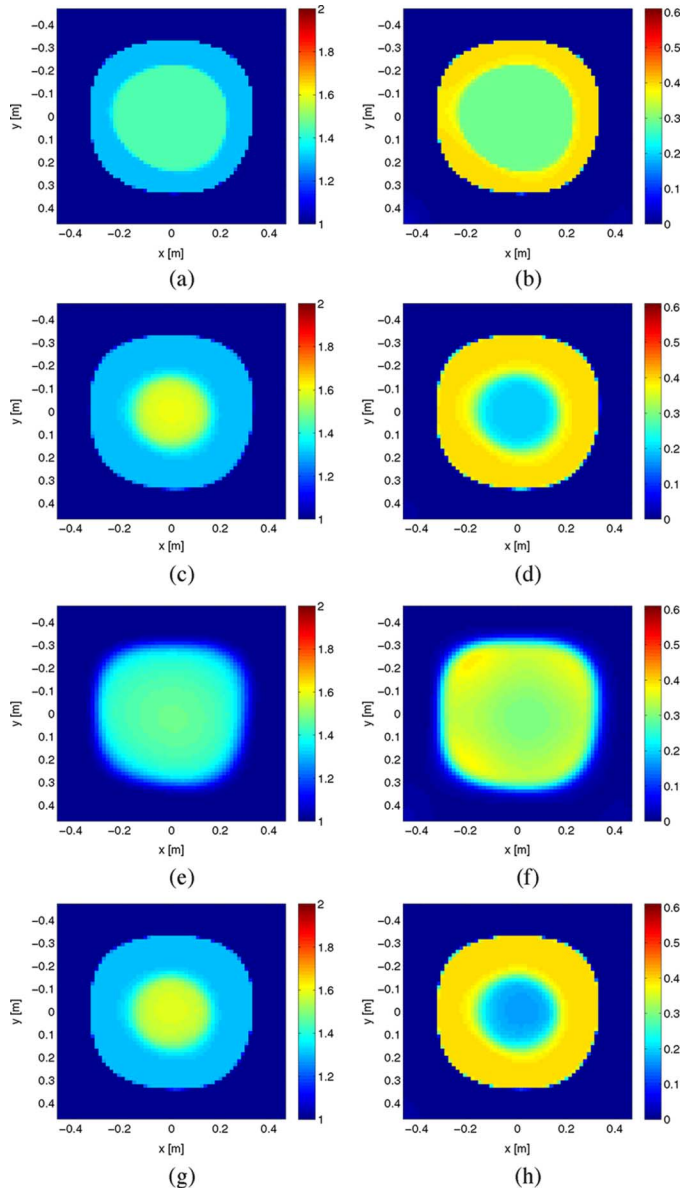

Fig. 5. The SL-GNI reconstruction of the concentric squares at $f = 100$ MHz when the *a priori* information about the number of contrast values L is wrong [left: $\mathrm{Re}(\epsilon_r)$ and right: $\mathrm{Im}(\epsilon_r)$]. Case I: In addition to the three true contrast values $\chi_1^{\mathrm{h}} = 0$, $\chi_2^{\mathrm{h}} = 0.6 + j0.2$, and $\chi_3^{\mathrm{h}} = 0.3 + j0.4$, one extra contrast value χ_4^{h} is also given to the SL-GNI algorithm: (a)–(b) $\chi_4^{\mathrm{h}} = 0.45 + j0.3$, and (c)–(d) $\chi_4^{\mathrm{h}} = 0.9 + j0.6$. Case II: Only two contrast values are given to the SL-GNI algorithm: (e)–(f) χ_1^{h} and χ_2^{h}, and (g)-(h) χ_1^{h} and χ_3^{h}.

responding to the target; i.e., utilizing a binary inversion algorithm instead of a trinary inversion algorithm. In Fig. 5(e)–(h), we have shown the performance of the SL-GNI algorithm for this situation for two sets of binary values at $f = 100$ MHz. Giving χ_1^{h} and χ_2^{h} to the SL-GNI algorithm, the reconstruction result does not resolve the two scatterers. This inversion result is, in fact, similar to the blind inversion of this data set [see Fig. 2(a)–(b)]. Giving χ_1^{h} and χ_3^{h} to the SL-GNI algorithm, the algorithm does resolve the two scatterers and provides a reconstruction result which is very similar to the one obtained using the three true contrast values [see Fig. 2(c)–(d)]. These two different cases show that the SL-GNI algorithm can be very sensitive to the utilized values for χ_ℓ^{h} if L is chosen to be a wrong number. As the focus of this paper is for the case where the correct value of L is known, we will not consider this case anymore. The usefulness of this algorithm when L is not known requires further study and is not within the scope of this paper.

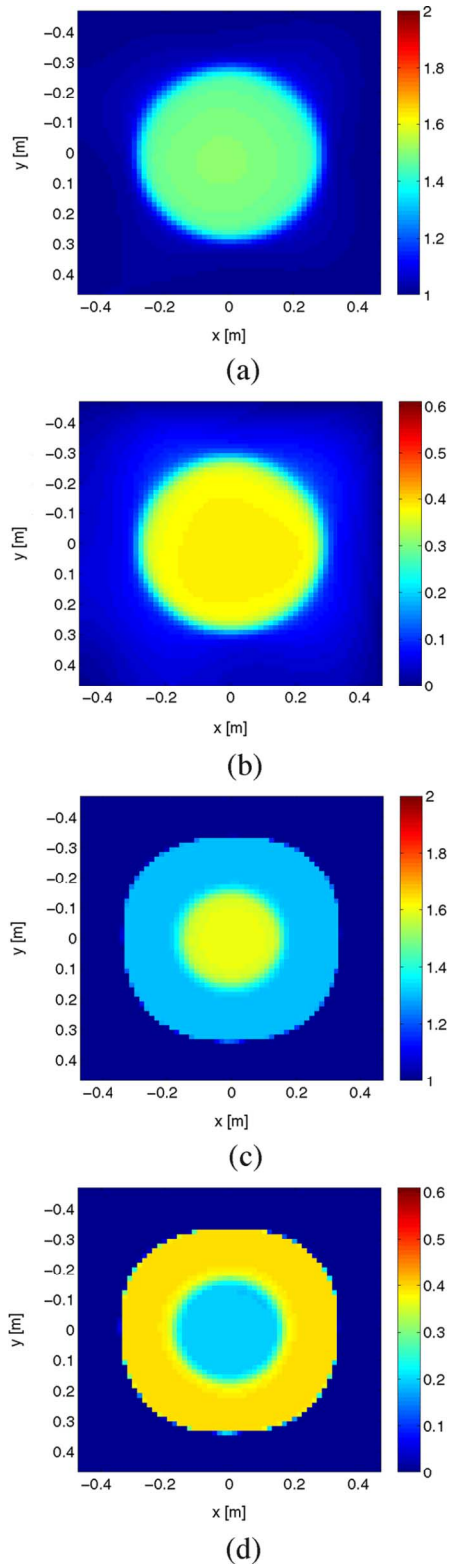

Fig. 6. Reconstruction of $\mathrm{Re}(\epsilon_r)$ and $\mathrm{Im}(\epsilon_r)$ of the concentric squares when illuminated by 32 transceivers at $f = 100$ MHz: (a)–(b) MR-GNI reconstruction, and (c)–(d) SL-GNI reconstruction.

To see if any changes can be observed in the reconstruction result of the first scenario ($f = 100$ MHz) using denser near-field sampling, the concentric squares are illuminated with 32 transmitters and the resulting scattered field is collected at 32 receivers per transmitter, thus, providing 32×32 data points (as opposed to 16×16 data points considered earlier). The reconstruction results using this new data set are shown in Fig. 6 for MR-GNI and SL-GNI. Comparing Fig. 6 with Fig. 2, it can be seen that only slight changes can be observed in the reconstruction results of this target by increasing the number of data points on the measurement circle. Thus, we speculate that we have reached the maximum amount of information that these two algorithms can extract from the given target at this specific frequency when the measured data, contaminated by 3% noise, is collected on the given measurement circle. That is, we speculate that increasing the number of transceivers from 16 to 32 has added redundant scattering information about this target for the given configurations. It should also be noted that although it is, in general, advantageous to increase the number of data points by having more coresident transmitters and receivers, it is in direct conflict with another design criteria which is the minimization of the mutual coupling between the coresident antenna elements [19, Ch. 7], [20]. That is also one of the reasons why the state-of-the-art microwave breast cancer imaging system at Dartmouth College utilizes only 16 monopole antennas [21]. Our microwave tomography system utilizes 24 Vivaldi antennas. Even with 24 Vivaldi antennas, we were not able to image at some frequencies due to the high mutual coupling between the coresident antenna elements at those frequencies [20].

TABLE I
NUMBER OF SL-GNI AND MR-GNI ITERATIONS REQUIRED FOR THE CONVERGENCE OF THE FIRST SYNTHETIC DATA SET IN SOME REPRESENTATIVE SCENARIOS

Example corresponding to	SL-GNI	MR-GNI
Fig. 2 (a) and (b)	-	8
Fig. 2 (c) and (d)	11	-
Fig. 3 (a) and (b)	-	18
Fig. 3 (c) and (d)	12	-
Fig. 4 (a) and (b)	8	-
Fig. 4 (c) and (d)	9	-

Finally, the number of iterations for this synthetic example in some representative scenarios is given in Table I. The main criterion governing the number of iterations is the difference between two successive data misfit values: if the difference between two successive data misfit values becomes less than 10^{-7}, the inversion algorithm is terminated.

B. 6-Ary Target

We consider the target shown in Fig. 7(a) and (b). The scatterer consists of a square having dimension of 0.03 m $\times$ 0.03 m with a relative complex permittivity of $4.5 + j4.5$ which is located inside a cylinder of diameter 0.07 m with a relative complex permittivity of $1.50 + j1.35$. Three smaller cylinders of diameter 0.031 m with three different relative complex permittivities, namely, $6 + j6$, $9 + j3$, and $7.5 + j1.5$, are located external to the larger cylinder. The background medium has a relative permittivity of 3 at the frequency of operation which is chosen to be 3 GHz. The target is interrogated using 32 transmitters (line sources) and 32 receivers which are evenly placed on the measurement circle $\mathcal{S}$ of radius 0.12 m. The synthetic data are then generated using a grid of 100×100 square pulses

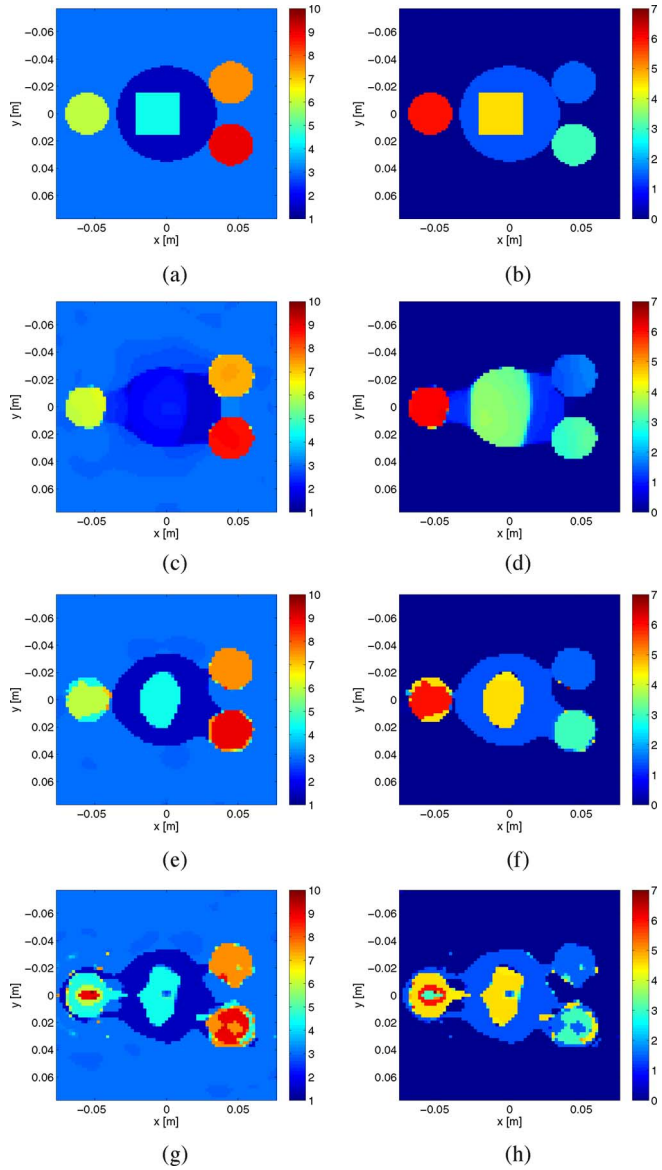

Fig. 7. The 6-ary target [left: $\mathrm{Re}(\epsilon_r)$ and right: $\mathrm{Im}(\epsilon_r)$]: (a)–(b) the true relative complex permittivity profile, (c)–(d) the MR-GNI reconstruction, (e)–(f) the SL-GNI reconstruction, and (g)–(h) the shape and location reconstruction method without the use of $\mathcal{C}_n^{\mathrm{MR}}$.

in a 0.15 m × 0.15 m square. The imaging domain $\mathcal{D}$ is chosen to be a 0.154 m × 0.154 m and is discretized into 71 × 71 square pulses.

The MR-GNI reconstruction of this target is shown in Fig. 7(c) and (d). As can be seen, the square has not been resolved in the MR-GNI real-part reconstruction. The MR-GNI imaginary-part reconstruction shows the presence of the square scatterer within the large cylinder; however, its dimension is very different than the true size of the square scatterer (i.e., 0.03 m × 0.03 m). The SL-GNI reconstruction of this target utilizing the contrast of zero as well as the five true contrast values of the scatterer is shown in Fig. 7(e) and (f). As can be seen, both real- and imaginary-part reconstructions resolve the square scatterer. Although the shape of the square scatterer is not reconstructed, its location and its approximate size have been reconstructed well. It is worth noting that if we remove the regularization term $\mathcal{C}_n^{\mathrm{MR}}$ from (11) and minimize $\mathcal{C}^{\mathrm{LS}}(\chi)\mathcal{C}_n^{\mathrm{hom}}(\chi)$ over the contrast (as opposed to minimizing $\mathcal{C}^{\mathrm{LS}}(\chi)\mathcal{C}_n^{\mathrm{hom}}(\chi)\mathcal{C}_n^{\mathrm{MR}}(\chi)$ over the contrast), the reconstruction result, shown in Fig. 7(g) and (h), is not satisfactory.

VI. Experimental Data Results

We consider two different experimental data sets. The first one is the *FoamDielIntTM* data set from the second Fresnel experimental data set [22] collected by the Institut Fresnel, France. The second data set is collected from the University of Manitoba air-filled microwave tomography system [20]. In both cases, the measured data are calibrated for the TM polarization so that the antennas can be represented by 2-D line sources. The calibration procedure adopted to calibrate the Fresnel data set is that explained in [23]. The calibration method utilized to calibrate the University of Manitoba data set is outlined in [20]. Similar to the inversion of synthetic data sets, the starting guess for the contrast to be found is set be zero in both MR-GNI and SL-GNI algorithms.

A. The Second Fresnel Data Set: FoamDielIntTM

For this data set, the transmitting and receiving antennas are both wide-band ridged horn antennas and are located on a circle with radius 1.67 m. The target [see Fig. 8(a)] consists of a lossless cylinder of diameter 0.031 m with the relative permittivity of 3 ± 0.3 which is located inside another lossless cylinder of diameter 0.08 m with the relative permittivity of 1.45 ± 0.15. This target is illuminated from eight different transmitter locations and the scattered data are collected at 241 locations per transmitter. The background medium is free space and the frequency of operation is chosen to be 3 GHz. The imaging domain $\mathcal{D}$ is a 0.15 m × 0.15 m square and is discretized into 60 × 60 square pulses.

The MR-GNI reconstruction of this single-frequency data set is shown in Fig. 8(b) and (c). Although the MR-GNI algorithm resolves the two different cylinders, the periphery of the outer cylinder is blurred, thus, it is difficult to deduce its radius from the reconstructed image. The SL-GNI reconstruction of this target using three values for χ^{h}, namely, $\chi_1^{\mathrm{h}} = 0$, $\chi_2^{\mathrm{h}} = 2$, and $\chi_3^{\mathrm{h}} = 0.45$, is shown in Fig. 8(d) and (e). As can be seen, the periphery of both circles is very clear. Also, the reconstructed radii for both cylinders are very accurate: the radius of the reconstructed outer cylinder is ≈0.078 m and that of the reconstructed inner cylinder is ≈0.03 m. We also run the SL-GNI algorithm with +20% error in the utilized values for χ^{h}. That is, the corresponding values of χ^{h} for the two cylinders utilized in the SL-GNI algorithm are chosen to be 2.4 and 0.54. The contrast of zero, which is the contrast of the background medium, is kept to be zero. The SL-GNI reconstruction results using these values for χ^{h} are shown in Fig. 8(f) and (g). As can be seen, the two cylinders are resolved. However, the radii of the inner cylinder and outer cylinders are underestimated: ≈0.024 m and ≈0.073 m. Finally, we note that all of these reconstructions show artifacts in the reconstructed imaginary parts. These artifacts are emphasized in the SL-GNI reconstructions at the boundary of the two cylinders. However, in the MR-GNI reconstruction, this artifact contains the whole inner cylinder but with a smaller magnitude compared to the magnitude of the artifact in the SL-GNI reconstruction. Finally,

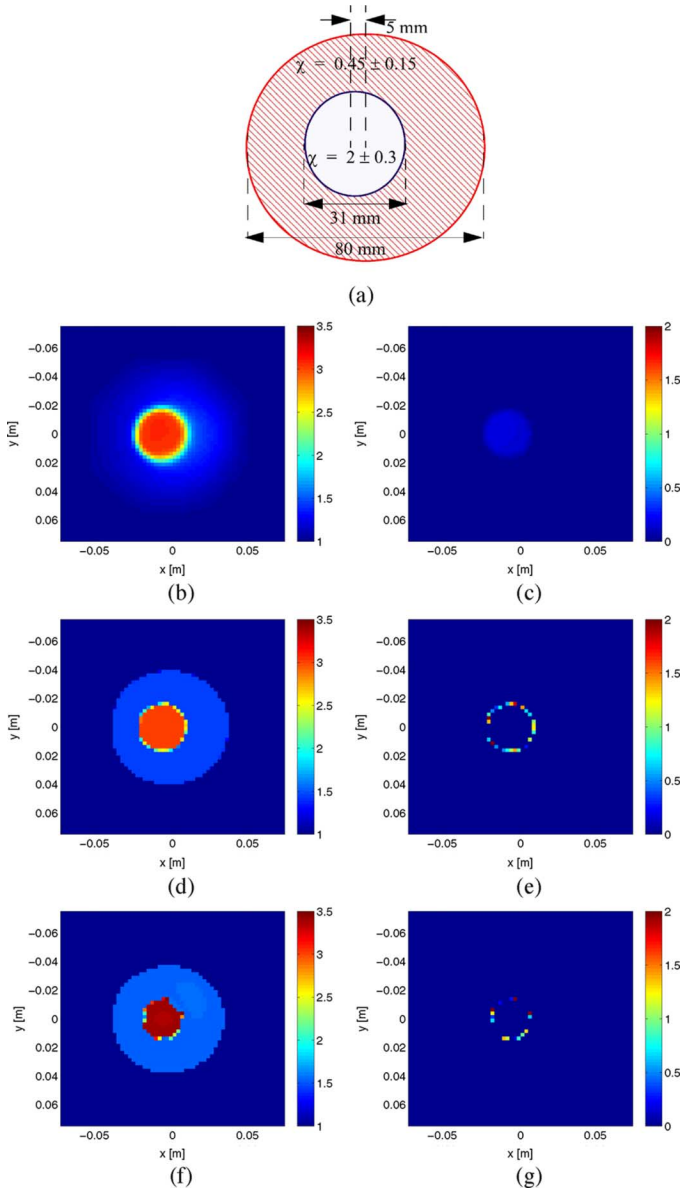

Fig. 8. (a) The *FoamDielIntTM* target from the second Fresnel experimental data set (frequency of operation is $f = 3$ GHz). Reconstruction [left: $\mathrm{Re}(\epsilon_r)$ and right: $\mathrm{Im}(\epsilon_r)$] using (b)–(c) the MR-GNI method, (d)–(e) the SL-GNI method, and (f)–(g) the SL-GNI method with 20% error in the utilized values for χ_ℓ^{h}.

TABLE II
NUMBER OF SL-GNI AND MR-GNI ITERATIONS REQUIRED FOR THE CONVERGENCE OF THE FIRST EXPERIMENTAL DATA SET

Example corresponding to	SL-GNI	MR-GNI
Fig. 7 (b) and (c)	-	9
Fig. 7 (d) and (e)	14	-
Fig. 7 (f) and (g)	21	-

the number of iterations for this experimental example is given in Table II.

B. Two Nylon Rods

This data set is collected using 24 co-resident Vivaldi antennas. The measured data are calibrated assuming that the radius of the measurement domain is 13.5 cm. Similar to [24], the two canonical targets are nylon-66 cylinders, 0.038 m in diameter and 0.44 m in height. The two cylinders were placed in the imaging system with the separation of the two targets being 8 mm as shown in Fig. 9. The background medium is free space and the frequency of operation is 5 GHz. Thus, this separation corresponds to $2\lambda_b/15$ where λ_b is the wavelength in the background medium. For each active transmitter, the scattered data are collected using the remaining antennas. That is, the measured data consist of 24×23 data points. At 5 GHz, the nylon has a measured relative complex permittivity of $\epsilon_r \approx 3.03 + j0.03$. The imaging domain $\mathcal{D}$ is chosen to be 0.104 m $\times$ 0.104 m and is discretized into 60×60 square pulses.

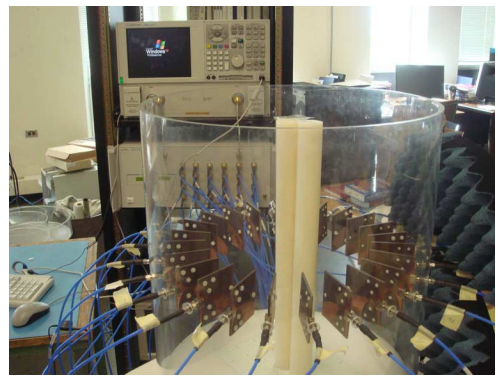

Fig. 9. University of Manitoba's microwave tomography system with two nylon cylinders with a separation of 8 mm (frequency of operation is $f = 5$ GHz).

The MR-GNI reconstruction of this target is shown in Fig. 10(a) and (b). As can be seen, these two cylinders are resolved and their reconstructed real-part permittivity value is very close to its expected value. However, the imaginary part of the permittivity profile has not been reconstructed due to its very small value and the limited signal-to-noise ratio of the measured data. The SL-GNI reconstruction of this target with two values for χ^{h}, namely, 0 and 2, is shown in Fig. 10(c) and (d). Similar to the MR-GNI reconstruction, the nylon rods are resolved. It is worth noting that the number of MR-GNI and SL-GNI iterations required for the convergence is 10 and 21; the first iterations of the MR-GNI and SL-GNI algorithms took about 17 and 13 s, respectively. To check whether the SL-GNI reconstruction is capable of reconstructing the very small imaginary part of the permittivity profile, we have run the SL-GNI algorithm with $\chi_1^{\mathrm{h}} = 0$ and $\chi_2^{\mathrm{h}} = 2.03 + j0.03$. However, it was still not able to reconstruct the imaginary part (not shown here). It should be noted that the SL-GNI algorithm used for this target may be referred to as a binary inversion algorithm as it deals with two different contrast values: the contrast of the background medium (which is zero) and that of the nylon rods. It is worth noting that if we remove the regularization term $\mathcal{C}_n^{\mathrm{MR}}$ from (11) and optimize $\mathcal{C}^{\mathrm{LS}}(\chi)\mathcal{C}_n^{\mathrm{hom}}(\chi)$ over χ, the reconstruction result, which is shown in Fig. 10(e) and (f), is not satisfactory.

To show the performance of the SL-GNI algorithm when the utilized χ^{h} for nylon rods contains a high error, we run the SL-GNI algorithm with 50% error in the utilized χ^{h} for the two nylon rods. That is, we assume that the contrast of the nylon

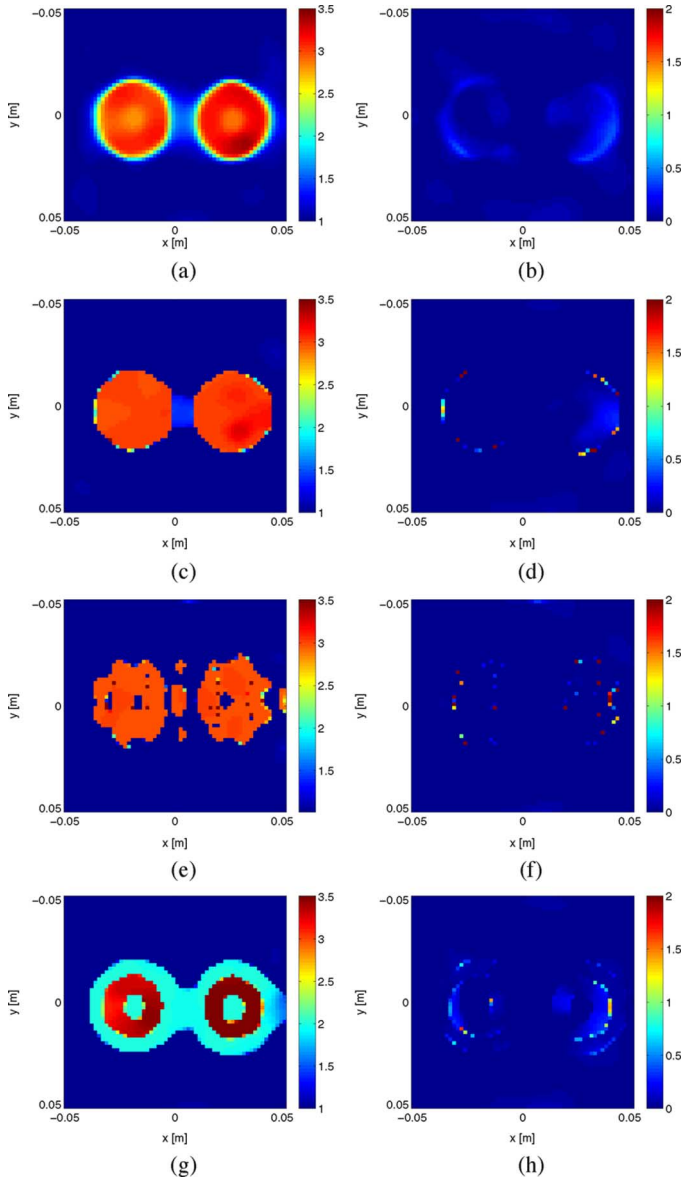

Fig. 10. The reconstructed relative complex permittivity of the two nylon cylinders [left: $\mathrm{Re}(\epsilon_r)$ and right: $\mathrm{Im}(\epsilon_r)$] using (a)–(b) the MR-GNI method, (c)–(d) the SL-GNI method, (e)–(f) the shape and location reconstruction method without the use of $\mathcal{C}_n^{\mathrm{MR}}$, (g)–(h) the SL-GNI method with 50% error in the utilized value for χ_ℓ^{h}.

rods is 1 (instead of 2). Using this wrong value, the SL-GNI reconstruction of the target is shown in Fig. 10(g) and (h). Although the SL-GNI algorithm was not capable of reconstructing the target with this utilized χ^{h} for the nylon rods, it shows that this value of χ^{h} is wrong. This can be deduced by noting that the reconstructed image shows three totally different contrast values: 1) contrast of zero (background medium), 2) contrast of 1, and 3) contrast of 2.5. This is in contradiction with the *a priori* information which assumes only one contrast value for the scatterers.

VII. Conclusion

We have presented a multiplicative regularized Gauss–Newton inversion algorithm for shape and location reconstruction which utilizes *a priori* information about the permittivity values of the objects being imaged. Using synthetically and experimentally collected data, we have shown that this algorithm is robust and can outperform the standard multiplicative regularized Gauss–Newton inversion algorithm in reconstruction the shape and location of the object of interest.

Appendix I
Derivative Operators

Herein, we derive the derivatives for $\mathcal{C}_n^{\mathrm{hom}}$ given in (10). The derivatives for $\mathcal{C}^{\mathrm{LS}}$ and $\mathcal{C}_n^{\mathrm{MR}}$ can be found in [12, App. D]. The derivatives for the regularized cost functional $\mathcal{C}_n^{\mathrm{shape}}$ can then be obtained using the product rule. We denote the L_2 spaces of complex functions defined on $\mathcal{D}$ by $L_2(\mathcal{D})$ with the norms and inner products defined as

$$\|\psi\|_{\mathcal{D}} = \langle \psi, \psi \rangle_{\mathcal{D}}^{1/2} \quad \text{and} \quad \langle \psi, \varphi \rangle_{\mathcal{D}} = \int_{\mathcal{D}} \psi(\boldsymbol{r}) \varphi^*(\boldsymbol{r}) d\boldsymbol{r} \quad (17)$$

where the superscript $*$ denotes the complex conjugate operator.

At the nth iteration of the GNI algorithm, we start with finding the limit

$$\lim_{\epsilon \to 0} \frac{\mathcal{C}_n^{\mathrm{hom}}(\chi_n + \epsilon\psi) - \mathcal{C}_n^{\mathrm{hom}}(\chi_n)}{\epsilon}. \quad (18)$$

The above limit can be written as

$$\lim_{\epsilon \to 0} \frac{1}{A\epsilon} \int_{\mathcal{D}} \prod_{\ell=1}^{L} \xi_{\ell,n}^2(\boldsymbol{r}) \left(\left| \chi_n(\boldsymbol{r}) + \epsilon\psi(\boldsymbol{r}) - \chi_\ell^{\mathrm{h}} \right|^2 + \alpha_n^2 \right) - \prod_{\ell=1}^{L} \xi_{\ell,n}^2(\boldsymbol{r}) \left(\left| \chi_n(\boldsymbol{r}) - \chi_\ell^{\mathrm{h}} \right|^2 + \alpha_n^2 \right) d\boldsymbol{r}. \quad (19)$$

The above limit can be simplified to (the argument $\boldsymbol{r}$ has been dropped for simplicity)

$$\lim_{\epsilon \to 0} \frac{1}{A\epsilon} \int_{\mathcal{D}} \prod_{\ell=1}^{L} \xi_{\ell,n}^2 \left(2\epsilon \mathrm{Re} \left\{ \left(\chi_n - \chi_\ell^{\mathrm{h}} \right) \psi^* \right\} + \left| \chi_n - \chi_\ell^{\mathrm{h}} \right|^2 + \alpha_n^2 \right) - \prod_{\ell=1}^{L} \xi_{\ell,n}^2 \left(\left| \chi_n - \chi_\ell^{\mathrm{h}} \right|^2 + \alpha_n^2 \right) d\boldsymbol{r}. \quad (20)$$

After mathematical simplifications, this can be written as

$$\frac{2}{A} \int_{\mathcal{D}} \sum_{\ell=1}^{L} \left[\xi_{\ell,n}^2 \mathrm{Re} \left\{ \left(\chi_n - \chi_\ell^{\mathrm{h}} \right) \psi^* \right\} \times \prod_{\ell' = \{1,\ldots,L\} - \{\ell\}} \left\{ \xi_{\ell',n}^2 \left(\left| \chi_n - \chi_{\ell'}^{\mathrm{h}} \right|^2 + \alpha_n^2 \right) \right\} \right] d\boldsymbol{r}. \quad (21)$$

Noting that

$$\xi_{\ell',n}^2 \left(\left| \chi_n - \chi_{\ell'}^{\mathrm{h}} \right|^2 + \alpha_n^2 \right) = 1 \quad (22)$$

expression (21) may be written as

$$\frac{2}{A} \sum_{\ell=1}^{L} \xi_{\ell,n}^2 \mathrm{Re} \left\langle \chi_n - \chi_\ell^{\mathrm{h}}, \psi \right\rangle_{\mathcal{D}}. \quad (23)$$

Writing the above limit as

$$\left\langle \frac{1}{A}\sum_{\ell=1}^{L}\xi_{\ell,n}^{2}\left(\chi_n-\chi_\ell^{\mathrm{h}}\right),\psi\right\rangle_{\mathcal{D}} + \left\langle \frac{1}{A}\sum_{\ell=1}^{L}\xi_{\ell,n}^{2}\left(\chi_n-\chi_\ell^{\mathrm{h}}\right)^{*},\psi^{*}\right\rangle_{\mathcal{D}} \tag{24}$$

the derivative operators may then be written as

$$\left.\frac{\partial\tilde{\mathcal{C}}_n^{\mathrm{hom}}}{\partial\chi}\right|_{\chi=\chi_n}(\psi)=\left\langle \frac{1}{A}\sum_{\ell=1}^{L}\xi_{\ell,n}^{2}\left(\chi_n-\chi_\ell^{\mathrm{h}}\right)^{*},\psi^{*}\right\rangle_{\mathcal{D}} \tag{25}$$

and

$$\left.\frac{\partial\tilde{\mathcal{C}}_n^{\mathrm{hom}}}{\partial\chi^{*}}\right|_{\chi=\chi_n}(\psi^{*})=\left\langle \frac{1}{A}\sum_{l=1}^{L}\xi_{\ell,n}^{2}\left(\chi_n-\chi_\ell^{\mathrm{h}}\right),\psi\right\rangle_{\mathcal{D}} \tag{26}$$

where $\tilde{\mathcal{C}}_n^{\mathrm{hom}}(\chi,\chi^{*})=\mathcal{C}_n^{\mathrm{hom}}(\chi)$. We note that $\tilde{\mathcal{C}}_n^{\mathrm{hom}}$ is an auxiliary cost functional which treats χ and χ^{*} as two independent functions. The cost functional $\tilde{\mathcal{C}}_n^{\mathrm{hom}}$ is complex differentiable with respect to χ for a fixed χ^{*} and *vice versa*. This method, sometimes referred to as Wirtinger calculus [25]–[28], [12, App. C], is one way of handling the fact that $\mathcal{C}_n^{\mathrm{hom}}$ is not complex differentiable with respect to the complex function χ.

To find the derivatives

$$\left[\left.\frac{\partial^2\tilde{\mathcal{C}}_n^{\mathrm{hom}}}{\partial\chi^{*}\partial\chi}\right|_{\chi=\chi_n}(\varphi)\right](\psi^{*})$$

and

$$\left[\left.\frac{\partial^2\tilde{\mathcal{C}}_n^{\mathrm{hom}}}{\partial\chi\partial\chi}\right|_{\chi=\chi_n}(\varphi)\right](\psi)$$

we start with finding the limit

$$\lim_{\epsilon\to 0}\frac{\left.\frac{\partial\tilde{\mathcal{C}}_n^{\mathrm{hom}}}{\partial\chi}\right|_{\chi=\chi_n+\epsilon\psi}(\varphi)-\left.\frac{\partial\tilde{\mathcal{C}}_n^{\mathrm{hom}}}{\partial\chi}\right|_{\chi=\chi_n}(\varphi)}{\epsilon}. \tag{27}$$

Utilizing (25), the above limit may be written as

$$\lim_{\epsilon\to 0}\frac{1}{\epsilon}\left[\left\langle \frac{1}{A}\sum_{\ell=1}^{L}\xi_{\ell,n}^{2}\left(\chi_n+\epsilon\psi-\chi_\ell^{\mathrm{h}}\right)^{*},\varphi^{*}\right\rangle_{\mathcal{D}} - \left\langle \frac{1}{A}\sum_{\ell=1}^{L}\xi_{\ell,n}^{2}\left(\chi_n-\chi_\ell^{\mathrm{h}}\right)^{*},\varphi^{*}\right\rangle_{\mathcal{D}}\right] \tag{28}$$

which can be simplified as

$$\left\langle \frac{1}{A}\sum_{\ell=1}^{L}\xi_{\ell,n}^{2}\psi^{*},\varphi^{*}\right\rangle_{\mathcal{D}}. \tag{29}$$

Writing the above expression as

$$\left\langle \frac{1}{A}\sum_{\ell=1}^{L}\xi_{\ell,n}^{2}\varphi,\psi\right\rangle_{\mathcal{D}} \tag{30}$$

it can be concluded that

$$\left[\left.\frac{\partial^2\tilde{\mathcal{C}}_n^{\mathrm{hom}}}{\partial\chi^{*}\partial\chi}\right|_{\chi=\chi_n}(\varphi)\right](\psi^{*})=\left\langle \frac{1}{A}\sum_{\ell=1}^{L}\xi_{\ell,n}^{2}\varphi,\psi\right\rangle_{\mathcal{D}} \tag{31}$$

and

$$\left[\left.\frac{\partial^2\tilde{\mathcal{C}}_n^{\mathrm{hom}}}{\partial\chi\partial\chi}\right|_{\chi=\chi_n}(\varphi)\right](\psi)=0. \tag{32}$$

Using a similar procedure, we can derive

$$\left[\left.\frac{\partial^2\tilde{\mathcal{C}}_n^{\mathrm{hom}}}{\partial\chi\partial\chi^{*}}\right|_{\chi=\chi_n}(\varphi^{*})\right](\psi)=\left\langle \frac{1}{A}\sum_{\ell=1}^{L}\xi_{\ell,n}^{2}\varphi,\psi\right\rangle_{\mathcal{D}}^{*} \tag{33}$$

and

$$\left[\left.\frac{\partial^2\tilde{\mathcal{C}}_n^{\mathrm{hom}}}{\partial\chi^{*}\partial\chi^{*}}\right|_{\chi=\chi_n}(\varphi^{*})\right](\psi^{*})=0. \tag{34}$$

Having found the derivative operators in the continuous domain, the discretized forms of these operators can easily be found. For example, the discretized form of (25) can be written as

$$\left[\left.\frac{\partial\tilde{\mathcal{C}}_n^{\mathrm{hom}}}{\partial\underline{\chi}^{*}}\right|_{\underline{\chi}_n}\right]^{T}\underline{\psi}^{*}=\left[\sum_{\ell=1}^{L}\underline{\boldsymbol{D}}_{\ell,n}\left(\underline{\chi}_n-\chi_\ell^{\mathrm{h}}\underline{e}\right)\right]^{T}\underline{\psi}^{*} \tag{35}$$

where the superscript "T" denotes the transposition operator.

The SL-GNI method also requires the derivatives of $\mathcal{C}_n^{\mathrm{MR}}$ and $\mathcal{C}^{\mathrm{LS}}$ with respect to χ and χ^{*}. Using the same procedure as explained above, these derivatives can be derived. The closed-form expressions of these derivative operators are given in [12, App. D]. Using the first-order derivative operators in the discrete domain, we can form the gradient of the cost functional $\mathcal{C}_n^{\mathrm{shape}}$ which is the negative of the vector given in the right-hand side of (13). To form the Hessian matrix, i.e., the matrix in the left-hand side of (13), we use the product rule. However, only the second derivative operators which make the Hessian matrix nonnegative definite are kept.

Appendix II
Oversampling of the Contrast

The proposed algorithm is robust with respect to oversampling of the unknown contrast. This can be explained as follows. Assume that we have a discrete ill-posed problem as $\underline{\boldsymbol{A}}\underline{x}=\underline{b}$ where $\underline{\boldsymbol{A}}\in\mathbb{C}^{m\times n}$, $\underline{b}\in\mathbb{C}^{m}$, and the unknown vector $\underline{x}$ is in $\mathbb{C}^{n}$. (In our problem, m is the number of measured data and n is the number of discretized elements in the imaging domain.) To solve this ill-posed problem, we use multiplicative regularization. It can be shown that multiplicative regularization when applied to the discrete ill-posed problem is equivalent to the following minimization [7, Sec. V]:

$$\underline{x}_\lambda=\arg\min_{\underline{x}}\{\|\underline{\boldsymbol{A}}\underline{x}-\underline{b}\|^2+\lambda\|\underline{\boldsymbol{R}}(\underline{x}+\underline{x}_0)\|^2\} \tag{36}$$

where $\underline{\underline{\boldsymbol{R}}} \in \mathbb{C}^{n\times n}$ is the regularization operator, λ is the regularization weight, and $\underline{x}_0 \in \mathbb{C}^n$ is some form of the initial guess (which is equal to the reconstructed contrast at the previous iteration of the GNI algorithm [7]). The above minimization is then equivalent to solving the following damped least squares problem:

$$\underline{x}_\lambda = \arg\min_{\underline{x}} \left\{ \left\| \begin{pmatrix} \underline{\underline{\boldsymbol{A}}} \\ \sqrt{\lambda}\underline{\underline{\boldsymbol{R}}} \end{pmatrix} \underline{x} - \begin{pmatrix} \underline{b} \\ -\sqrt{\lambda}\underline{\underline{\boldsymbol{R}}}\,\underline{x}_0 \end{pmatrix} \right\|^2 \right\}. \quad (37)$$

As can be seen in (37), the unknown vector $\underline{x}$ belongs to $\mathbb{C}^n$ whereas the matrix $\begin{pmatrix} \underline{\underline{\boldsymbol{A}}} \\ \sqrt{\lambda}\underline{\underline{\boldsymbol{R}}} \end{pmatrix}$ belongs to $\mathbb{C}^{(m+n)\times n}$. Thus, whatever we choose the number of discretized elements in the imaging domain (i.e., n), the number of rows of the matrix $\begin{pmatrix} \underline{\underline{\boldsymbol{A}}} \\ \sqrt{\lambda}\underline{\underline{\boldsymbol{R}}} \end{pmatrix}$ will be more than the number of elements in the vector $\underline{x}$. This makes the algorithm robust to oversampling of the unknown contrast.

ACKNOWLEDGMENT

The authors would like to thank the Institut Fresnel, France, for providing the *FoamDielIntTM* experimental data set.

REFERENCES

[1] A. Abubakar, T. Habashy, V. Druskin, L. Knizhnerman, and D. Alumbaugh, "2.5D forward and inverse modeling for interpreting low-frequency electromagnetic measurements," *Geophysics*, vol. 73, no. 4, pp. F165–F177, Jul.–Aug. 2008.

[2] P. Meaney, N. Yagnamurthy, and K. D. Paulsen, "Pre-scaled two-parameter Gauss-Newton image reconstruction to reduce property recovery imbalance," *Phys. Med. Biol.*, vol. 47, pp. 1101–1119, 2002.

[3] A. Abubakar and P. M. van den Berg, "The contrast source inversion method for location and shape reconstructions," *Inverse Probl.*, vol. 18, pp. 495–510, 2002.

[4] L. Crocco and T. Isernia, "Inverse scattering with real data: Detecting and imaging homogeneous dielectric objects," *Inverse Probl.*, vol. 17, pp. 1573–1583, 2001.

[5] K. Belkebir, R. Kleinman, and C. Pichot, "Microwave imaging-location and shape reconstruction from multifrequency scattering data," *IEEE Trans. Microw. Theory Tech.*, vol. 45, no. 4, pp. 469–476, Apr. 1997.

[6] K. Belkebir, C. Pichot, J. C. Bolomey, P. Berthaud, G. Cottard, X. Derobert, and G. Fauchoux, "Microwave tomography system for reinforced concrete structures," in *Proc. 24th Eur. Conf.* , 1994, vol. 2, pp. 1209–1211.

[7] P. Mojabi and J. LoVetri, "Overview and classification of some regularization techniques for the Gauss-Newton inversion method applied to inverse scattering problems," *IEEE Trans. Antennas Propag.*, vol. 57, no. 9, pp. 2658–2665, Sep. 2009.

[8] A. Abubakar, P. M. van den Berg, and J. J. Mallorqui, "Imaging of biomedical data using a multiplicative regularized contrast source inversion method," *IEEE Trans. Microw. Theory Tech.*, vol. 50, no. 7, pp. 1761–1777, Jul. 2002.

[9] P. Mojabi and J. LoVetri, "Microwave biomedical imaging using the multiplicative regularized Gauss-Newton inversion," *IEEE Antennas Wireless Propag. Lett.*, vol. 8, pp. 645–648, 2009.

[10] P. Mojabi and J. LoVetri, "A novel microwave tomography system using a rotatable conductive enclosure," *IEEE Trans. Antennas Propag.*, vol. 59, no. 5, pp. 1597–1605, May 2011.

[11] P. Charbonnier, L. Blanc-Féraud, G. Aubert, and M. Barlaud, "Deterministic edge-preserving regularization in computed imaging," *IEEE Trans. Image Process.*, vol. 6, no. 2, pp. 298–311, Feb. 1997.

[12] P. Mojabi, "Investigation and development of algorithms and techniques for microwave tomography" Ph.D. dissertation, Dept. Electr. Comput. Eng., Univ. Manitoba, Winnipeg, MB, Canada, 2010 [Online]. Available: http://mspace.lib.umanitoba.ca/handle/1993/3946

[13] T. M. Habashy and A. Abubakar, "A general framework for constraint minimization for the inversion of electromagnetic measurements," *Progr. Electromagn. Res.*, vol. 46, pp. 265–312, 2004.

[14] P. Mojabi and J. LoVetri, "Comparison of TE and TM inversions in the framework of the Gauss-Newton method," *IEEE Trans. Antennas Propag.*, vol. 58, no. 4, pp. 1336–1348, Apr. 2010.

[15] A. Abubakar, P. M. van den Berg, and S. Y. Semenov, "A robust iterative method for Born inversion," *IEEE Trans. Geosci. Remote Sens.*, vol. 42, no. 2, pp. 342–354, Feb. 2004.

[16] P. M. van den Berg and R. E. Kleinman, "A contrast source inversion method," *Inverse Probl.*, vol. 13, pp. 1607–1620, 1997.

[17] P. M. van den Berg, A. L. van Broekhoven, and A. Abubakar, "Extended contrast source inversion," *Inverse Probl.*, vol. 15, pp. 1325–1344, 1999.

[18] B. J. Kooij and P. M. van den Berg, "Nonlinear inversion in TE scattering," *IEEE Trans. Microw. Theory Tech.*, vol. 46, no. 11, pp. 1704–1712, Nov. 1998.

[19] J. Stang, "A 3D active microwave imaging system for breast cancer screening," Ph.D. dissertation, Dept. Electr. Comput. Eng., Duke Univ., Durham, NC, 2008.

[20] C. Gilmore, P. Mojabi, A. Zakaria, M. Ostadrahimi, C. Kaye, S. Noghanian, L. Shafai, S. Pistorius, and J. LoVetri, "A wideband microwave tomography system with a novel frequency selection procedure," *IEEE Trans. Biomed. Eng.*, vol. 57, no. 4, pp. 894–904, Apr. 2010.

[21] T. Rubæk, P. M. Meaney, P. Meincke, and K. D. Paulsen, "Nonlinear microwave imaging for breast-cancer screening using Gauss-Newton's method and the CGLS inversion algorithm," *IEEE Trans. Antennas Propag.*, vol. 55, no. 8, pp. 2320–2331, Aug. 2007.

[22] J.-M. Geffrin, P. Sabouroux, and C. Eyraud, "Free space experimental scattering database continuation: Experimental set-up and measurement precision," *Inverse Probl.*, vol. 21, pp. S117–S130, 2005.

[23] R. F. Bloemenkamp, A. Abubakar, and P. M. van den Berg, "Inversion of experimental multi-frequency data using the contrast source inversion method," *Inverse Probl.*, vol. 17, pp. 1611–1622, 2001.

[24] C. Gilmore, P. Mojabi, A. Zakaria, S. Pistorius, and J. LoVetri, "On super-resolution with an experimental microwave tomography system," *IEEE Antennas Wireless Propag. Lett.*, vol. 9, pp. 393–396, 2010.

[25] W. Wirtinger, "Zur formalen theorie der funktionen von mehr komplexen veränderlichen," *Mathematische Annalen*, vol. 97, no. 1, pp. 357–375, 1927.

[26] H. Li and T. Adali, "Complex-valued adaptive signal processing using nonlinear functions," *EURASIP J. Adv. Signal Process.*, 2008, DOI: 10.1155/2008/765615.

[27] D. H. Brandwood, "A complex gradient operator and its application in adaptive array theory," *Inst. Electr. Eng. Proc. F and H*, vol. 130, no. 1, pp. 11–16, 1983.

[28] A. van den Bos, "Complex gradient and Hessian," *Inst. Electr. Eng. Proc.—Vision Image Signal Process.*, vol. 141, no. 6, pp. 380–383, 1994.

Puyan Mojabi (S'09–M'10) received the B.Sc. degree in electrical engineering from the University of Tehran, Tehran, Iran, in 2002, the M.Sc. degree in electrical engineering from Iran University of Science and Technology, Tehran, Iran, in 2004, and the Ph.D. degree in electrical engineering from the University of Manitoba, Winnipeg, MB, Canada, in 2010.

He is currently an Assistant Professor with the Electrical and Computer Engineering Department, University of Manitoba. His current research interests are computational electromagnetics, antenna design, and inverse problems.

Joe LoVetri (S'84–M'84–SM'09) was born in Enna, Italy, in 1963. He received the B.Sc. (with distinction) and M.Sc. degrees, both in electrical engineering, from the University of Manitoba, Winnipeg, MB, Canada, in 1984 and 1987, respectively, and the Ph.D. degree in electrical engineering from the University of Ottawa, Ottawa, ON, Canada, in 1991.

From 1984 to 1986 he was EMI/EMC Engineer at Sperry Defence Division, Winnipeg, MB, Canada. From 1986 to 1988, he held the position of TEMPEST Engineer at the Communications Security Establishment, Ottawa, ON, Canada. From 1988 to 1991, he was a Research Officer at the Institute for Information Technology, National Research Council of Canada. From 1991 to 1999, he was an Associate Professor in the Department of Electrical and Computer Engineering, The University of Western Ontario, London, ON, Canada. In 1997–1998 he spent a sabbatical year at the TNO Physics and Electronics Laboratory, The Netherlands. Since 1999, he has been a Professor in the Department of Electrical and Computer Engineering, University of Manitoba, and was Associate Dean, Research, from 2004 to 2009. His main interests lie in time-domain computational electromagnetics, modeling of electromagnetic compatibility problems, microwave tomography, and inverse problems.

Lotfollah Shafai (S'67–M'69–SM'75–F'88–LF'07) received the B.Sc. degree from the University of Tehran, Tehran, Iran, in 1963 and the M.Sc. and Ph.D. degrees from the Faculty of Applied Sciences and Engineering, University of Toronto, Toronto, ON, Canada, in 1966 and 1969, respectively, all in electrical engineering.

In November 1969, he joined the Department of Electrical and Computer Engineering, University of Manitoba, Winnipeg, MB, Canada, as a Sessional Lecturer, Assistant Professor (1970), Associate Professor (1973), and Professor (1979). Since 1975, he has made special effort to link the University research to the industrial development, by assisting industries in the development of new products or establishing new technologies. To enhance the University of Manitoba contact with industry, in 1985 he assisted in establishing "The Institute for Technology Development," and was its Director until 1987, when he became the Head of the Electrical Engineering Department. His assistance to industry was instrumental in establishing an Industrial Research Chair in Applied Electromagnetics at the University of Manitoba in 1989, which he held until July 1994.

Dr. Shafai has been a participant in nearly all antennas and propagation symposia and participates in the review committees. He is a member of Commission B of the International Union of Radio Science (URSI) and was its Chairman during 1985–1988. In 1986, he established the Symposium on Antenna Technology and Applied Electromagnetics (ANTEM) at the University of Manitoba that is currently held every two years. He has been the recipient of numerous awards. In 1978, his contribution to the design of a small ground station for the Hermus satellite was selected as the Third Meritorious Industrial Design. In 1984, he received the Professional Engineers Merit Award, and in 1985, "The Thinker" Award from Canadian Patents and Development Corporation. From the University of Manitoba, he received the "Research Awards" in 1983, 1987, and 1989, the Outreach Award in 1987 and the Sigma Xi, Senior Scientist Award in 1989. In 1990, he received the Maxwell Premium Award from the Institution of Electrical Engineers (IEE; London, U.K.), and in 1993 and 1994, the Distinguished Achievement Awards from Corporate Higher Education Forum. In 1998, he received the Winnipeg RH Institute Foundation Medal for Excellence in Research. In 1999 and 2000, he received the University of Manitoba, Faculty Association Research Award. He was elected a Fellow of The Royal Society of Canada in 1998. He was a recipient of the IEEE Third Millennium Medal in 2000, and in 2002, was elected a Fellow of The Canadian Academy of Engineering and Distinguished Professor at The University of Manitoba. In 2003, he received an IEEE Canada "Reginald A. Fessenden Medal" for "outstanding contributions to telecommunications and satellite communications," and a Natural Sciences and Engineering Research Council (NSERC) Synergy Award for "development of advanced satellite and wireless antennas." He holds a Canada Research Chair in Applied Electromagnetics and was the International Chair of Commission B of URSI for 2005–2008. In 2009, he was elected a Fellow of the Engineering Institute of Canada, and was the recipient of an IEEE Chen-To-Tai Distinguished Educator Award. In 2011, he received a Killam Prize in Engineering from The Canada Council for the Arts, for his "outstanding Canadian career achievements in engineering, and his work in antenna research."